Chapter 4
Manipulation and Spectroscopy Using AFM/STM at Room Temperature

Masayuki Abe, Yoshiaki Sugimoto and Seizo Morita

Abstract In the atom manipulation process with atomic force microscopy (AFM) at room temperature, reduction of the local energy barrier induced by interaction forces between atoms of a tip and a surface plays a key role. This means that the force value depending on the tip-apex condition determines the success of manipulation. In the first part of this chapter, the probability of the AFM atom manipulation is discussed. It is found that the value of the maximum attractive force, i.e. the tip reactivity, determines the manipulation capability. In addition, the potential barrier reduction can be used for various purposes such as local chemical reactions, barrier height control of the potential of nanospace, and fabrication of atomic-sized materials (i.e., nanoclusters). In the second part of the chapter, nanoclusters are fabricated as an application of the AFM atom manipulation. Half-unit cells of the Si(111)-(7 × 7) are used as a nanospace for structuring the atomic-sized clusters.

4.1 Introduction

Atomic force microscopy (AFM) is an important tool for characterizing various nanostructures and sample surfaces, including insulators. Stable acquisition of atomic resolution images can now be achieved using the frequency modulation technique [1],

M. Abe (✉)
Center for Science and Technology Under Extreme Conditions,
Graduate School of Engineering Science, Osaka University,
1-3, Machikaneyama-Cho, Toyonaka, Osaka 560-8531, Japan
e-mail: abe@stec.es.osaka-u.ac.jp

Y. Sugimoto
Department of Electrical, Electronic and Information Engineering,
Graduate School of Engineering, Osaka University, Yamada-Oka 2-1,
Suita 565-0871, Japan
e-mail: sugimoto@afm.eei.eng.osaka-u.ac.jp

S. Morita
Nanoscience and Nanotechnology Center, The Institute of Scientific and Industrial Research,
Osaka University, 8-1 Mihogaoka, Ibaraki, Osaka 567-0047, Japan
e-mail: smorita@eei.eng.osaka-u.ac.jp

S. Morita et al. (eds.), *Noncontact Atomic Force Microscopy*,
NanoScience and Technology, DOI 10.1007/978-3-319-15588-3_4

wherein a cantilever is oscillated at its resonance frequency (f_0), and the frequency shift (Δf) caused by the tip-surface interaction force is detected [2, 3]. As an application of the frequency modulation AFM, measurement of the tip-surface distance dependence of the Δf (so-called force spectroscopy) [4] enables analysis of single-atom chemical properties [5, 6].

Atom manipulation using AFM [7–17] has recently become a fascinating area of research, since the AFM manipulation experiments can be performed not only at low temperature but also at room temperature. Another attractive feature of the AFM atom manipulation is that the AFM can measure the driving forces involved in the atom manipulation process at the same time. Ternes et al. manipulated metal adsorbates on a metal surface at low temperature, and concluded that the lateral force acting on the AFM tip determined the manipulation process [9]. Conversely, on semiconductor surfaces at room temperature, the vertical force plays a dominant role [8]. This striking difference was attributed to the presence of highly directional covalent bonds on semiconductor surfaces. The measurements of forces during the manipulation process have provided the signatures of specific mechanical atom manipulation processes [8, 9, 14, 18]. In the attractive tip-sample interaction regime, reduction of the local energy barrier between atoms induced by interaction forces between the tip and surface atoms was found to be a key in the manipulation process (Fig. 4.1) [8, 18–20]. Surface atoms do not move to a neighboring site unless the tip reduces the surface potential barrier sufficiently for the surface atom to "hop".

From a slightly different perspective, reduction of the potential barrier can be used for various purposes, such as local chemical reactions and height control of the potential of nanospaces, and fabrication of atomic-sized materials (i.e., nanoclusters). Scanning tunneling microscopy (STM) has been used to create atomic-sized structures [21] at low temperature. This method has also been applied for the creation of various artificial nanostructures in an atom-by-atom fashion [22–25]. It has been proven that AFM could be used for the atomic-size creation even at room temperature [26]. Despite these achievements, the assembly of well-defined clusters exhibiting high thermal stability at room temperature and precise determination of the cluster size remain challenging tasks [27]. More importantly, the assembly of nanoclusters

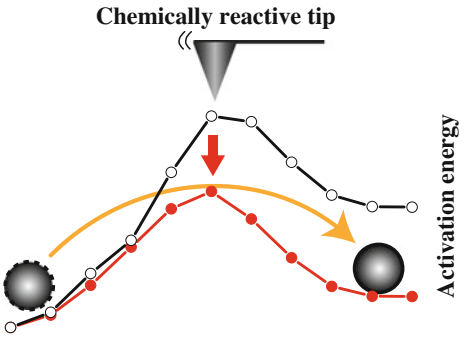

Fig. 4.1 Principle model for explaining the atom manipulation using atomic force microscopy (AFM) at room temperature

from multi-elements at room temperature has not been demonstrated, despite the wide potential range of technical applications for such assembly.

In the first part of this chapter, the probability of atom manipulation is discussed. Attractive force maxima over the Si adatoms are measured using a large variety of tips, and their relations to the manipulation probability at room-temperature are investigated. We found that the atom manipulation capability and its efficiency in the manipulation process are strongly dependent on the maximal force of a tip acting on the Si adatom. It is also found that the tip reactivity determines not only the manipulation capability but also the spatial resolution of AFM. In the second part of this chapter, as an application of the AFM atom manipulation, we propose a novel technique to assemble various atom clusters composed of a defined number of atoms at room temperature. Half-unit cells of the Si(111)-(7 × 7) are used as nanospaces for structuring the atomic-sized clusters. By reducing the height of the potential barrier of the nanospace (i.e., the boundary of the Si(111)-(7 × 7) half-unit cell) in the attractive region, AFM tip opens the "gate" for an atom to move to a neighboring nanospace.

4.2 Relation Between Manipulation Probability and Tip Reactivity

In the AFM manipulation process, the tip-apex structure, orientation, and chemical nature influence the success rate [18]. For example, tip reactivities (i.e., the maximum attractive force of the AFM tip) are different even if same type cantilevers are used [5]. In order to increase the efficiency of the atomic manipulation process, a detailed understanding of the tips exhibiting different interaction characteristics is therefore required.

Here we will show the probability of displacing a Si adatom to a vacancy site on the Si(111)-(7 × 7) surface as a function of the tip-sample distance. The statistics of the lateral manipulation of Si adatoms for various processes are produced using many tips that span a broad range of attractive force maxima over the Si adatoms. It is shown that the atom manipulation capability and its efficiency in this particular manipulation process are strongly dependent on the maximal force of a tip acting on the Si adatom.

4.2.1 AFM Setup

The experiments were performed using a home-built ultrahigh-vacuum AFM operated at room temperature. The AFM operation mode used here was the frequency modulation (FM) detection [1], which we have previously used to perform atom manipulation experiments [8, 10, 26, 28]. Commercial Si cantilevers were cleaned

by Ar ion sputtering prior to the imaging and manipulation experiments to remove native oxide layers and other contaminants. A sample bias voltage (V_s) was applied so that the electrostatic force was minimized. Undesired tip-sample motion due to the thermal drift was compensated during the experiment at the appropriate time point: measurement of the drift velocity [29] and its use as a feedforward [30] parameter were performed. The thermal drift compensation enables us to perform room-temperature experiments of atom-manipulation and site-specific force spectroscopy with a lateral precision of 0.1 Å.

4.2.2 Vacancy Formation on the Si(111)-(7 × 7) Surface

For suitable atom manipulation experiments, we selected a center of terrace of the Si(111)-(7 × 7) surface. Since we need a vacancy to perform the experiment, as indicated by the drawing in Fig. 4.2a, we created a vacancy site by mechanical indentation [31]. The process for the vacancy creation is outlined below: we positioned the AFM tip over a Si adatom to be removed, and then opened the z feedback to close and retract the AFM tip from the Si surface by a certain displacement that was preliminarily input. If a vacancy was not created in the AFM image obtained just after the z displacement of the AFM tip, we repeated the same process with a gradual increment of the displacement until we found the vacancy. After repeated indentations, the tip apex may become unstable or a clear atomic resolution image may not been obtained. We moved the AFM tip position 10 nm laterally away from the vacancy site, and scanned it vertically until it became stable.

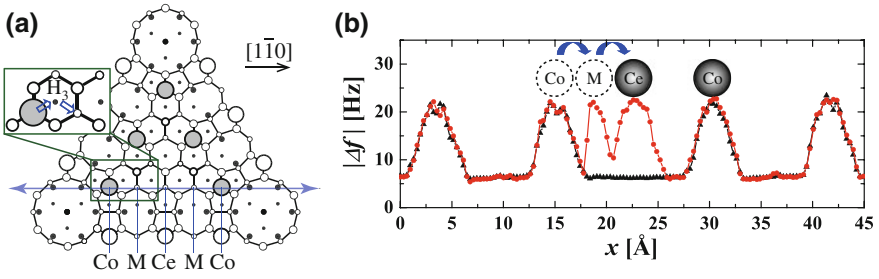

Fig. 4.2 **a** A schematic model of a half-unit cell of a Si(111)-(7 × 7) surface. *Gray circles* are Si adatoms, and a vacancy exists at the center (Ce) adatom site. The *zoom out* indicates the detail of the most favorable adatom hopping path from a corner (Co) adatom → a hollow site (H_3) → a meta stable (M) site. Successive forward and backward tip scans above the line connecting the two Co sites including the vacancy Ce site are carried out. **b** Two examples of Δf line profiles reveal the dynamics of the Si adatom during the manipulation process acquired with the same scan parameters. The *line profile* indicated with *triangles* does not show the atom hopping signature while the profile with *circles* shows atom hopping from a Co to a Ce site *via* the M site

4.2.3 Confirmation of Tip Reactivity

Since we know that, in previous studies, the tip approach reduced the potential barrier between two atomic sites in the room-temperature manipulation, the tip-apex condition determines the performance of the atom manipulation experiment. This is why, prior to the manipulation experiments, we performed force spectroscopic measurements above a Si adatom. The obtained distance-dependence curve of the frequency shift ($\Delta f - z$ curve) was inverted to force distance curve ($F - z$ curve) using Sader's method [32]. We eliminated long-range component from the inverted $F - z$ curve to obtain a short-range force (F_{SR}) having a high correlation with atomic resolution imaging. The maximum attractive value of F_{SR} varies even if the same commercial AFM tips are used [5]. This means that the chemical reactivity of the AFM tip is not the same.

4.2.4 Atom Manipulation Procedures

Atom manipulation requires precise adjustment of the scan line above the center of a vacancy and a target adatom. While the compensation of the thermal drift is activating, in order to manipulate a Si adatom to the vacancy site, we carried successive line scans above the line connecting the vacancy and the target adatom (in the $[1\bar{1}0]$ direction). Constant height scans where the tip-surface feedback was turned off were used to obtain reliable statistics on the atom manipulation procedure at well-defined distances. The Δf signal was recorded simultaneously during the scan. For control of the scan direction, we used a versatile scan controller [33]. Since the probability of adatom hopping to the adjacent vacancy side depends on the interaction force [8], we performed the manipulation line scan at different tip-sample distances to investigate the change of the manipulation probability. For example, when the line scan was performed as shown in Fig. 4.2a, we obtained two types of Δf line profiles in Fig. 4.2b. From these line profiles, we found two different outcomes starting from the same initial atom configuration. Even under the same scan conditions, there was a case that atom hopping occurred or not. In Fig. 4.2b, the profile with triangles does not show Δf at the Ce site, which means the Ce site is the vacancy. On the other hand, Δf with circles shows the existence of an adatom not only at the Ce site but also at the M site. This indicates that the Co adatom at the left side hops to the Ce site via the M site during the scan. After this process, the vacancy was located on the left Co site.

Figure 4.3(a_1–f_2) shows changes over time in the constant height Δf line profile. Successive line scans above the same line on the Si(111)-(7 × 7) surface along the $[1\bar{1}0]$ direction visualize the atom manipulation processes as images. We got the AFM tip closer to the surface in order to obtain the images $a_{1,2}$ to $f_{1,2}$. The subscript notation indicates the fast scan direction: the scan passes through from left to right (a_1–f_1) and right to left (a_2–f_2) along the $[1\bar{1}0]$ line. We emphasize that the tip apex did

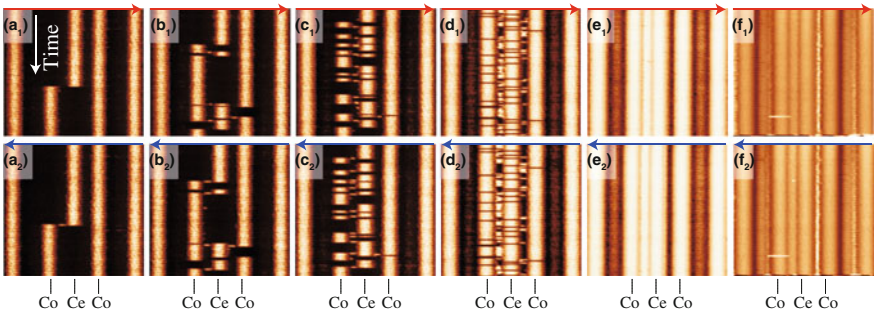

Fig. 4.3 Atom manipulation images composed by the successive line scan profiles (the constant height Δf) at different tip-sample distances. The *subscript notation* indicates the fast scan direction from *left* to *right* (a_1–f_1), and *right* to *left* (a_2–f_2). The tip-sample distances for data acquisition were $z = 0.21$ Å (a_1, a_2), $z = 0.12$ Å(b_1, b_2), $z = 0.02$ Å (c_1, c_2), $z = -0.17$ Å (d_1, d_2), $z = -0.31$ Å (e_1, e_2), and $z = -1.16$ Å (f_1, f_2). The z values were determined from the force curves acquired before the experiments shown here. $z = 0.0$ Å is defined at the distance where the force takes the minimum value

not change during this series of experiments. In the images, the bright and continuous stripes as well as the intermittent stripes in the Δf images indicate the position of the Si adatom during the manipulation processes. The success of the manipulation process could be inferred from the pattern of Δf images and from the line profiles.

The Si adatoms happened to change their adsorption locations among the corner adatom (Co), meta-stable (M), and center adatom (Ce) sites by interaction with the tip when the tip was repeatedly scanned at sufficiently small tip-surface distances along the same line. The probability of a change in the induced site due to the tip-sample interaction depends on the tip-sample distance under the same tip-apex condition. In Fig. 4.3, we observed various types of line profiles corresponding to different atom-hopping processes, meaning the stochastic nature of the hopping processes at room temperature [11]. Since a continuous stripe means that the tip manipulates the Si adatom at a high rate, a closer tip-sample distance has higher probability for the atom move.

4.2.5 Relation Between Measured Force and Atom Manipulation Probability

Analyses of the line profiles in Fig. 4.3 reveal the relation between the atom manipulation probability and the force acting on the tip apex. We analyzed more than 3000 line profiles to find the distance dependence of the probability, as shown in Fig. 4.4. Here, the probability is defined as the ratio of the number of successful atom movements to the total number of line scans (i.e., manipulation attempts), which are represented as a percentage. In Fig. 4.4, solid circles, open circles, and open triangles give atom

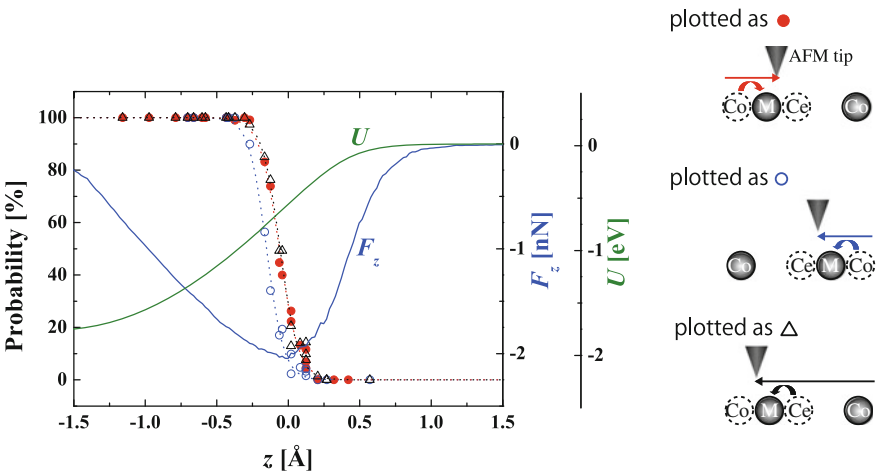

Fig. 4.4 Relation between atom manipulation probabilities and tip-sample distance from the *left* Co to the M site (*solid circles*), from the *right* Co to the M site (*open circles*), and from the Ce to the M site (*open triangles*). The plots are fitted to an empirical step function, $P(z) = 100/[1 + \exp[\alpha (z - z_0)]]$, where α is the thermal broadening coefficient and z_0 is defined as the distance for $P = 50\,\%$. $F_z(z)$ and $U(z)$ curves obtained above the Co adatom using the same tip are also shown. *Right side* figures indicate three types of the Si adatom hopping by tip scan

manipulation probabilities from the left Co to the M site, from the right Co to the M site, and from the Ce to the M site, respectively.

Each of these processes is illustrated schematically on the right side of Fig. 4.4. The short-range force curve $[F_z(z)]$ together with the potential energy curve $[U(z)]$ which are inverted from the $\Delta f(z)$ curve on a Co adatom are also indicated in Fig. 4.4. The $F_z(z)$ and $U(z)$ curves acquired over the Co adatom site are used as a reference for estimation of the tip-sample distances. Even in the attractive force region, the hopping probability is almost zero, but it drastically increases from 0 to 100 % at around the distance of the maximum attractive F_z region.

A comparison of the probability difference of the scan direction (solid plot as left-to-right tip scan, and open plots as right-to-left scan) revealed that the probability was also dependent on the scan direction, as shown in Fig. 4.4. The probability of atom movement from left to right along the Co to the M site is higher than the probability of movement from the right to the left. Since the manipulation pathways of both directions are symmetrical, the difference in probability should come from the tip asymmetry and/or the orientation of the tip-apex dangling bond with respect to the surface adatoms. The ability to vertically manipulate atoms on semiconductors depends strongly on the orientation of the dangling bonds at the tip apex with respect to the target atom [34]. This means that the directional difference in the dangling bond alignment with respect to the target atom leads to a variation of the manipulation probability.

By comparing the site difference with the same scan direction, it is found that the probability for adatom hopping from the Ce to the M site (triangles) is higher than that from the Co to the M site (open circles) at the same tip-surface distances. This difference results from the difference in the diffusion energy barrier. The results do not contradict previous experimental investigations based on adatom extraction [35] and displacement [36] acquired by applying a voltage pulse to the Si(111)-(7 × 7) surface. The above-described results, including those of the AFM manipulation in this chapter, suggest that a higher energy barrier is associated with the transition from the Co to the M site.

4.2.6 Tip Reactivity and Manipulation Capability

Although the probability of AFM atom manipulation depends on the tip-sample distance, there are AFM tips that can not move Si adatoms even at closer tip-sample distance. As shown in Fig. 4.5a, the probability of atom manipulation (solid circle) with this type of AFM tip continues to be zero even when the tip approaches the surface beyond the maximum attractive force region. But tip-apex modification due to gentle contact between the tip and sample does result in the probability change. Figure 4.5b shows the distance dependence of the manipulation probability after the gentle contact of the AFM tip of Fig. 4.5a. Although the same tip was used, the probability began to increase at the distance of the maximum attractive force due to the tip-apex change. It was found that the difference between before and after the gentle contact was the difference between the maximum attractive forces, which were ≈1.2 nN and ≈1.7 nN, respectively.

In order to investigate the relation between the manipulation capability and the maximum attractive force values, we performed the same experiment with 15 different states of the AFM tip apex using 10 cantilevers, where gentle tip contact with the sample surface enabled the tip apex to be in a different state. Figure 4.6 is a histogram of the maximum attractive forces measured above Si adatoms using 15 different tip

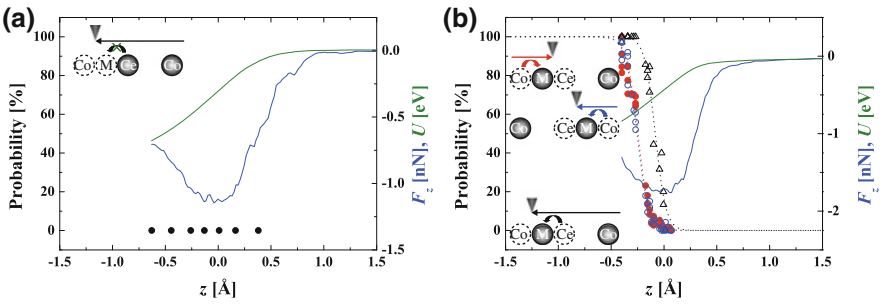

Fig. 4.5 **a** A case zero with manipulation probability in the whole measured region (*solid circle*). $F_z(z)$ and $U(z)$ are shown together to refer the tip-sample distance. The distance of the maximum attractive force is defined as $z = 0$ Å. **b** The same data set after the tip-apex modification done by gentle tip-sample contacts

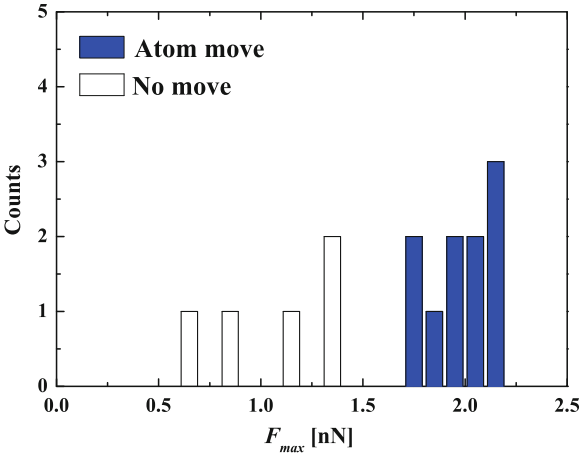

Fig. 4.6 Histogram of the maximum attractive forces measured above Si adatoms; the histogram was obtained using 15 different tips, and reveals the relationship between the magnitude of the maximum attractive force and the capability of atom manipulation

apexes. In the histogram, the solid and the white counted on each force values indicate whether or not the manipulation occurred, respectively. The histogram has wide distribution, but the capability of the atom manipulation separate distinctly at around ≈1.5 nN.[1] This means that the tip reactivity determines whether the tip can induce the manipulation: the Si adatoms can be manipulated with the reactive tips, but not with less-reactive tips.

4.2.7 Tip Reactivity and Spatial Resolution

The signatures attributed to the atom manipulation capabilities of the tips also appear in the AFM topographic images. Figure 4.7a, b shows AFM topographic images using the tips that can move the atom and those that can not, respectively. The tips of Fig. 4.7a, b have maximum attractive forces of ≈2.0 nN and ≈1.2 nN. The tip of Fig. 4.7b, which has no ability to manipulate Si adatoms, resolves the Si rest atoms together with adatoms.

4.3 Inter-nanospace Atom Manipulation for Structuring Nanoclusters

As a application field of the atom manipulation experiments, nanoclusters are of great importance in physics and chemistry as well as in technical applications, such as single electron transistors [39, 40], nanocatalysts [41–43], and quantum

[1] Such a broad dispersion of F_{max} can be attributed to the varying degrees of tip-apex chemical reactivity [37, 38].

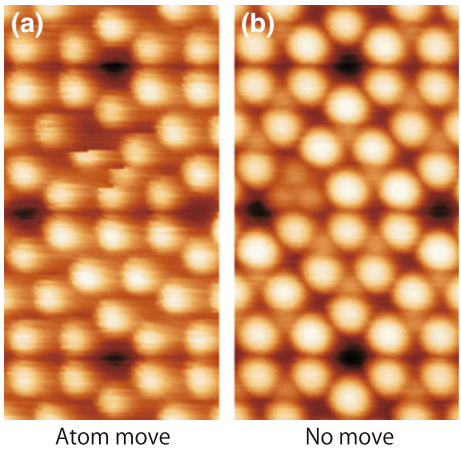

Fig. 4.7 AFM topographic images of Si(111)-(7 × 7) showing different spatial resolutions with different types of tip apex. In the experiment of **a** the AFM tip has a larger maximum attractive force (≈2.0 nN) and reduced the potential barrier until the atom manipulation occurred. With the AFM tip of **b** the Si adatom could not be moved, but rest atoms were resolved in imaging. The AFM tip has a smaller maximum attractive force (≈1.2 nN)

computing devices [44]. The properties of nanoclusters are highly sensitive to size and chemical composition. For example, Au clusters of nm-scale show size effects on catalytic behavior [41, 43]. For a fundamental understanding of atomically well-defined clusters, it is essential to control number of atoms. Although the cluster formation method allows us to obtain uniform cluster arrays [45, 46], one cannot determine the number of atoms involved in a cluster structure once they are deposited on surfaces.

Recently, we have demonstrated an alternative approach to fabrication of single nanoclusters using the same principle as used for AFM atom manipulation at room temperature (Inter-nanospace Atom Manipulation; INSAM) [47]. This method allows us to create nanoclusters with different chemical compositions and to evaluate their chemical stabilities. In this section, the assembly of various nanoclusters in an atom-by-atom fashion using the AFM at room temperature is shown. The method is based on the transfer of single diffusing atoms among nanospaces governed by "atomic gates," in which potential barriers are reduced by the AFM tip.

4.3.1 Method for Inter-nanospace Atom Manipulation

Figure 4.8 shows the concept of the INSAM process for fabricating a nanocluster. We consider that a small area is surrounded by a potential barrier, which is called a "nanospace" in this chapter. An adsorbate atom in the nanospace would move due to the thermal diffusion, but would not go over the barrier. In the INSAM operation, the approach of the AFM tip near the surface causes a decrease in the potential barrier,

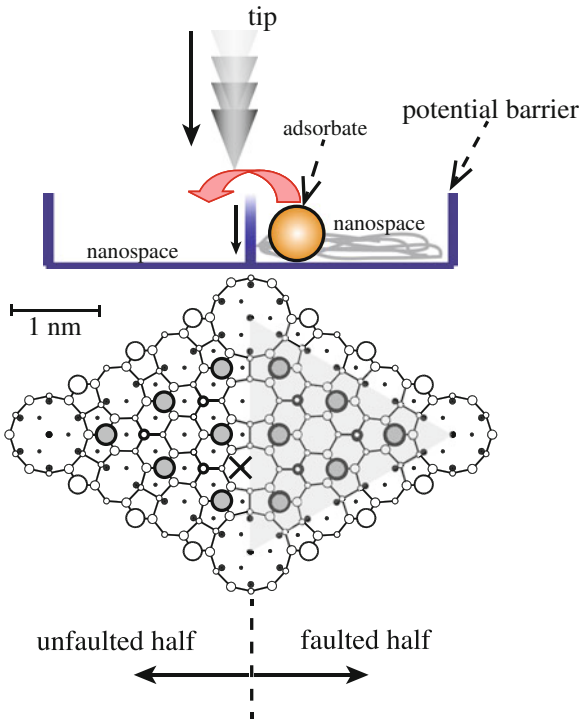

Fig. 4.8 Concept of Inter-nanospace Atom Manipulation (INSAM). The approach of the AFM tip near the surface reduces the potential barrier, allowing the adsorbed atom to "hop" to a neighboring nanospace. Here, we use half-unit cells of Si(111)-(7 × 7) as the nanospace

and thereby induces movement of the adsorbed atom to a neighboring nanospace. In the experiment described here, we used a half-unit cell in the Si(111)-(7 × 7) surface works as a nanospace of an equilateral triangle with side lengths of 2.7 nm. The adsorbate atom travels among the various potential minima in a nanospace. These minima are known to be multi-coordinate sites rather than the tops of Si adatoms and rest atom sites [48]. The successive INSAM operations allow us to assemble single atoms to the predetermined nanospace: we can control the number of atoms to configure nanoclusters. Further, various elements can be moved, and the relation between electronic and geometrical properties of nanoclusters can be investigated just after the fabrication using AFM/STM and other scanning probe techniques.

Given the fact that nanoclusters on surfaces have a wide range of applications, it becomes important to construct ordered and well-defined cluster arrays with a defined number of atoms. We expect that nanoclusters constructed from a well-determined number of atoms would provide evidence of the unique size-dependent properties.

4.3.2 AFM/STM Setup for the INSAM Operation

We performed the experiments for the INSAM method not only with AFM but also with STM and AFM/STM with metallic cantilever. The experiments were carried

out using an ultrahigh-vacuum AFM as mentioned in Sect. 4.2.1. Commercial Pt-Ir-coated Si cantilevers (NCLPt, NanoWorld) were used for the STM measurements. Metallic cantilevers can demonstrate conventional (static) STM measurement without cantilever oscillation. In the AFM/STM mode, the cantilevers need to be oscillated for AFM operation, so STM is operated in the dynamic mode. In the dynamic STM, the tunneling current flows instantaneously at a close tip-surface distance during cantilever oscillation. The time-averaged tunneling current ($\langle I_t \rangle$) is then detected, since the bandwidth of the current-to-voltage converter is usually much smaller than the resonance frequency of the cantilever [49]. A bias voltage (V_s) was applied to the sample with respect to the tip, which was virtually grounded using an operational amplifier. The tunneling current I_t signal was measured from the tip. Elements of Si, Sn, Pb, Ag, and Au were deposited onto the Si(111)-(7 × 7) surface to form the nanoclusters. The element deposition was performed by using a Joule heating evaporator in an ultra-high vacuum, while the Si sample temperature was kept at room temperature.

4.3.3 Inter-nanospace Atom Manipulation of Various Elements

Figure 4.9 shows STM (a–f) and AFM (g, h) images before and after the INSAM operation to various elements on the Si(111)-(7 × 7). Single atoms of Au (a → b), Ag (c → d), Pb (e → f), Sn (g → h) deposited on the Si(111)-(7 × 7) surface are imaged. In Fig. 4.9a, three single Au atoms are imaged: two of them are in the faulted half-unit cells and one is in the unfaulted half-unit cell. Three half-unit cells with Au atoms appear brighter than the half-unit cells without Au atoms. The contrast of the STM image of the two different half-unit cells (faulted and unfaulted) occupied by single Au atoms appears to be different. Corner (center) adatoms were imaged more brightly than center (corner) adatoms in the faulted half-unit cell (unfaulted half-unit cell) in the filled-state STM images. The results are consistent with the results of the previous studies [50, 51]. In the case of the other elements, the contrast of the faulted sites is different from that of the unfaulted sites. This difference in contrast is attributed to the electronic structure modifications and the topographic differences between the faulted and unfaulted sites. As is the case in Au atoms, the diffusion rate of the adsorbates in the nanospace is so large that an STM image cannot resolve the specific adsorption sites offered by the surface at room temperature [52]. And the different adsorbate atoms on the Si(111)-(7 × 7) appear differently in the STM images due to differences in the diffusion properties.

As the tip gradually approaches the position indicated by a cross in the Si(111)-(7 × 7) unit (a, c, e, g), the adsorbate atom moves to the neighboring half-unit cell (b, d, f, h). The approach was repeated until the diffusing atom was successfully transferred into the desired nanospace.

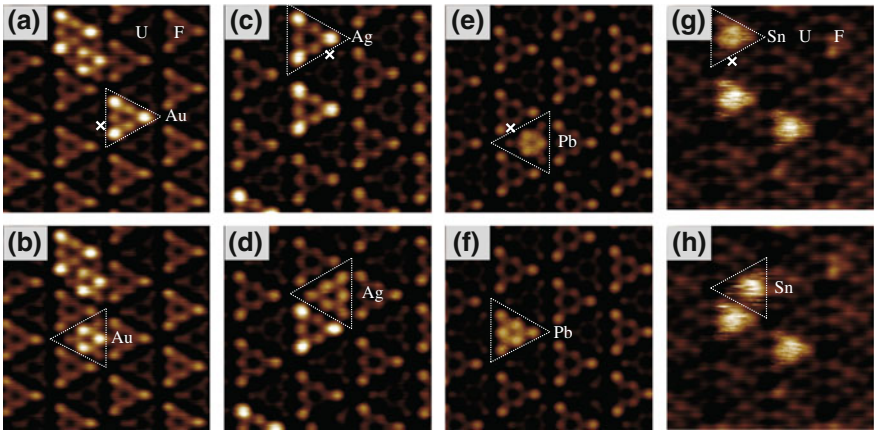

Fig. 4.9 STM (**a**–**f**) and AFM (**g**, **h**) images before and after the INSAM of various elements on the Si(111)-(7 × 7). The tip gradually approaches the position indicated by a cross in the Si(111)-(7 × 7) unit cell to move single atoms of Au (a → b), Ag (c → d), Pb (e → f), Sn (g → h). F and U denote faulted and unfaulted half unit cell, respectively. The bias voltage and the tunneling current set points for STM imaging are $V_s = -1000\,\mathrm{mV}$ and $I_t = 30\,\mathrm{pA}$ (**a**, **b**), 50 pA (**c**, **d**), and 40 pA (**e**, **f**), respectively. The bias voltage in the INSAM for Sn was $V_s = 0\,\mathrm{V}$. The acquisition parameters for AFM imaging were $f_0 = 153972.5\,\mathrm{Hz}$, $k = 25.2\,\mathrm{N/m}$, $A = 198\,\text{Å}$, and $\Delta f = -2.1\,\mathrm{Hz}$

The INSAM operations of g–h are performed with the 0 V bias voltage. The Sn atom can be successfully relocated into the predetermined nanospace using an AFM tip. This is strong evidence that the INSAM is caused by the mechanical (force) effects and not by tunneling current.

4.3.4 Fabrication of Nanocluster Using Inter-nanospace Atom Manipulation

Complex nanoclusters can be fabricated by repeating the INSAM operation. As an example, the assembly of Au_N clusters (N = 1–17) is demonstrated in Fig. 4.10. We fabricated these clusters by bringing single Au atoms into the predetermined nanospace one-by-one using the INSAM method. Atom-by-atom assembly allows us to study the dependence of the cluster stability on the size of clusters or the number of atoms that compose them. While Au_1–Au_3 clusters show quick thermal diffusion, Au_4 and Au_7–Au_{12} clusters retain stable structures, and no changes were observed in their appearance over several hours. The Au_5 and Au_6 clusters were relatively stable within the scanning time scale, but we confirmed the structure changes of Au_5 and Au_6. These changes occurred unexpectedly every several minutes to be conformations among equivalent forms by following the threefold and/or the mirror symmetry of the surface. A threefold symmetry contrast was obtained in STM images on Au_7–Au_{11} clusters. These clusters are similar to the self-assembled

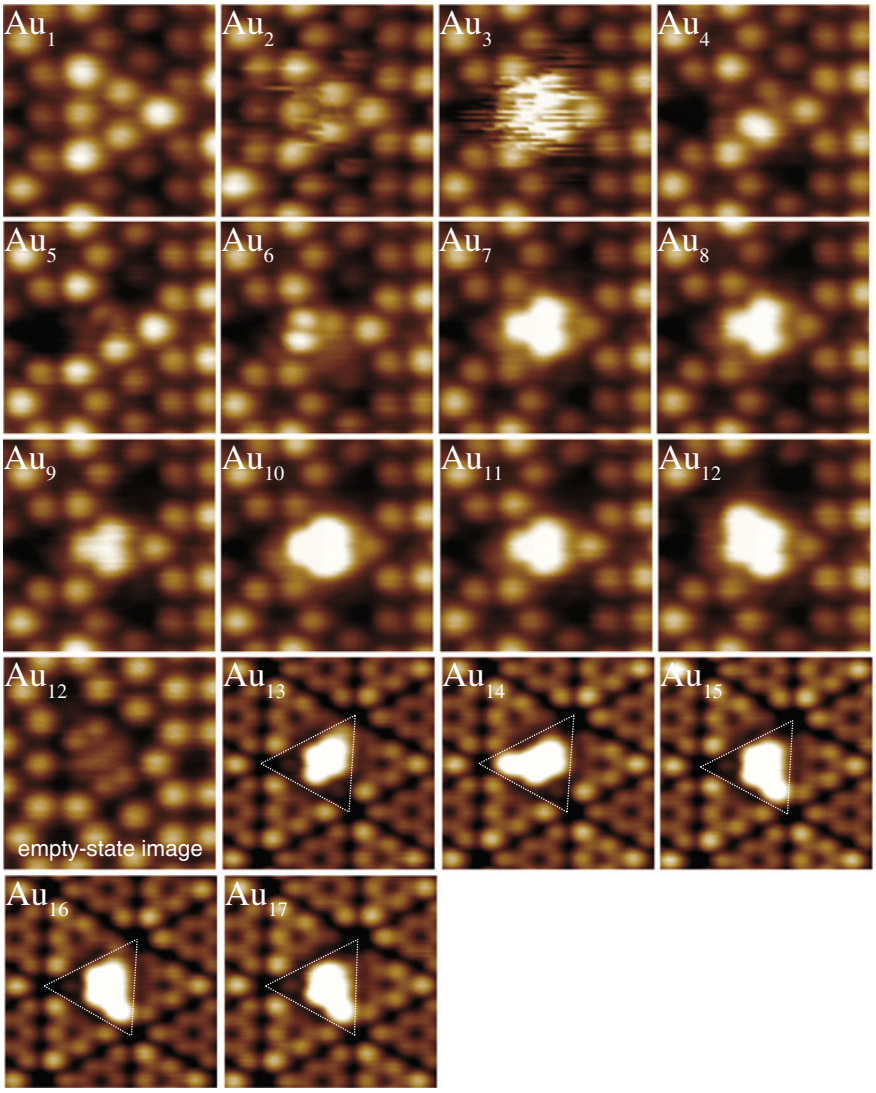

Fig. 4.10 Fabrication of Au atom clusters (Au_1–Au_{17}) using the INSAM method on the half unit cell of the Si(111)-(7 × 7) surface. The imaging parameters were $V_s = -500\,mV$ and $I_t = 30\,pA$ for Au_1–Au_{12} and $V_s = -1000\,mV$ and $I_t = 30\,pA$ for Au_{13}–Au_{17}. One of the Au_{12} STM images is acquired in the empty-state mode ($V_s = 1000\,mV$ and $I_t = 40\,pA$)

clusters observed previously [53, 54]. In contrast, the structure of Au_{12} did not retain the threefold symmetry. From both the filled- and empty-state STM images, we find that the Au_{12} structure has a mirror symmetry. By repeating it further, we finally succeeded in fabricating the Au_{17} cluster.

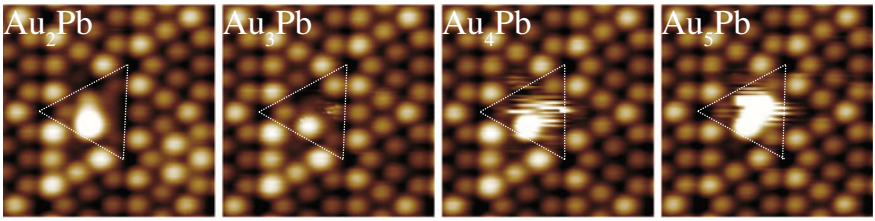

Fig. 4.11 STM images of multi-element atom clusters showing the influence of a single Pb atom on the stability of Au_2–Au_5 clusters assembled by atom gating control. The acquisition parameters were $V_s = -1000\,\mathrm{mV}$ and $I_t = 30\,\mathrm{pA}$

The INSAM operation can also be used to assemble multi-element clusters. The composition can be designed and controlled in the cluster in an atom-by-atom fashion. The images in Fig. 4.11 are bimetallic clusters involving metal atoms of two different species assembled using the INSAM operations. The presence of the single Pb atom in Au_2 can stabilize the Au_2Pb cluster, although Au_2 and Au_3 are mobile at room temperature. In contrast, the Au_4Pb and Au_5Pb clusters exhibit two distinct features separated by partially stable round and fuzzy features in the STM images, whereas Au_4–Au_6 are relatively stable (see Fig. 4.10). Details of the characteristics of clusters are described in [47].

4.3.5 Distance Spectroscopic Measurement During INSAM Operation

To understand the mechanisms underlying the INSAM operation, we performed force-distance spectroscopy acquired together with the INSAM operation using AFM/STM. Since the tip is closed to the surface to reduce the potential barrier in the INSAM operation, one can measure the distance dependence at the same time. The simultaneously measured distance dependence of the tunneling current (I_t), the energy dissipation, and the force during the INSAM operation of the Au atom are shown in Fig. 4.12. During the decrease in the tip-sample distance for the INSAM operation, I_t varies exponentially with distances (see the "Approach" curve in Fig. 4.12a). Then, discontinuous jumps are observed at $z = 0.3\,\text{Å}$ in all signals. This comes from an Au atom hop from the original nanospace to the neighboring nanospace located below the tip. Once the Au atom is transferred to the nanospace below the tip, trapping and release of the Au atom occurs repeatedly due to the large cantilever oscillation amplitude used in our experiments. The trap and release cycles of the Au atom should not happen when the closest tip-sample distance is out of the interaction region.

There are three distance regions in the distance curves, which are determined by the observed differences in their slopes: the trapping and release region ((i) $z \leq 1.2\,\text{Å}$),

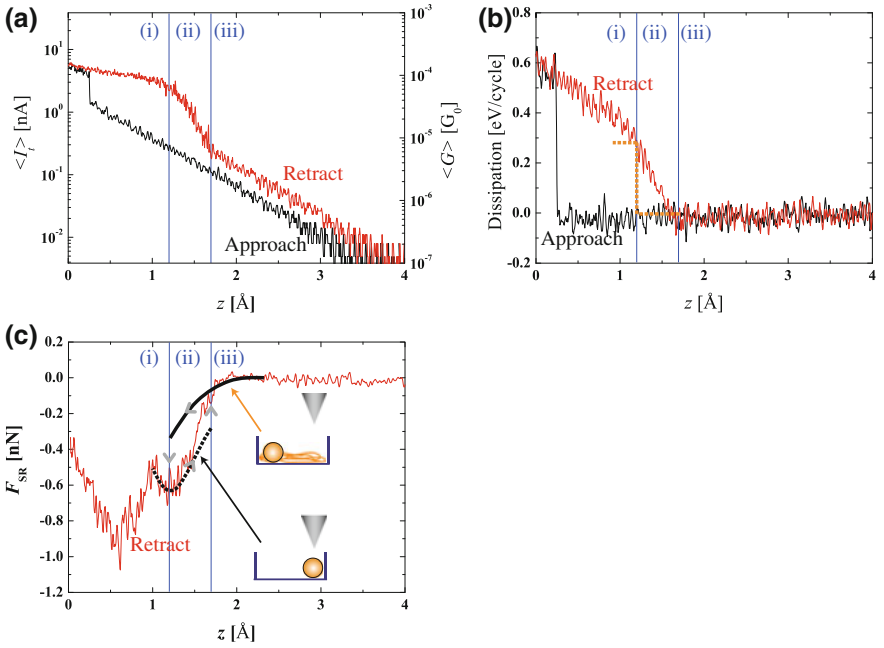

Fig. 4.12 Simultaneous measurements of **a** $\langle I_t(z) \rangle$ and **b** energy dissipation and **c** short-range force curves (F_{SR}) as a function of the tip-sample distance during the INSAM operation for the Au atom on the Si(111)-(7 × 7). The sample bias is $V_s = -500$ mV during the data acquisition. The short-range force was inverted from $\Delta f(z)$ [32] and the background long-range force was subtracted

the region of transition from contact to tunneling ((ii) $1.2 \leq z \leq 1.7$ Å), and the free diffusion region ((iii) $z \geq 1.7$ Å). In region (i), I_t decreases with smaller slope by increasing tip-sample distance. In this regime, the formation and collapse of the tip-Au-surface atomic junction are repeated for every tip oscillation cycle, and the ballistic current would flow through the junction at around the lowest tip point. In region (ii), the slope of the $I_t(z)$ curve is larger than that of region (i), and more importantly, the Au atom is not trapped in every cantilever oscillation cycle. The Au atom-trapping rate varies from 100 % at $z = 1.2$ Å to 0 % at $z = 1.7$ Å as the tip-sample distance increases. In regime (iii), there is no chemical bonding between the Au atom and the tip-apex atom, and the tip cannot trap the Au atom. Since the Au atom is not trapped, it thermally diffuses within the nanospace. In this region, I_t decreases exponentially by following the basic tunneling law. It is worth mentioning that, in this region, the $I_t(z)$ curves of approach and retraction do not match. The existence of the diffusing Au causes the difference: the topographic and electronic structure modifications induced by the Au atom diffusion on the surface enhance the tunneling current upon retraction.

The simultaneously measured energy dissipation also contains information on the dynamic evolution of the atomic junction during Au atom trapping and release.

Trapping and release during the INSAM in region (i) enhances the dissipation energy of the 0.6 eV/cycle (see Fig. 4.12b). The observed behavior can be attributed to the adhesion mechanism of dissipation, as previously proposed in [10, 55–58], where a double-well potential energy surface caused energy dissipation. In our studies, a hysteresis caused by the trapping and the release of the Au atom produces the dissipation signal. Since the atomic scale dissipation as observed in dynamic AFM is usually associated with instabilities at the tip-surface interface at close proximity [10, 57, 58], it is clear that the dissipation is caused by the trapping and release of the Au atom by the tip. This means that the observed enhancement of the dissipation signal is due to such structural rearrangements, and the triggering mechanism of the INSAM is a purely mechanical effect.

One can estimate, from short-range force (F_{SR}), the threshold force associated with the atom trapping and the chemical bonding force that can stabilize the atomic junction formed between the tip and surface. In region (iii), the Au atom diffuses freely without any tip trapping (see the inset in this region). At the boundary of regions (ii) and (iii), where the Au atom begins to diffuse (i.e., $z = 1.7$ Å), we were able to obtain this force value required to trap a single diffusing Au atom by the tip of -0.1 nN. And as the tip starts to trap/diffuse the Au atom, the dependence of the force distance begins to change. This force change is due to the existence of the Au atom trap. While the solid curve represents the force curve that is expected for the diffusing Au atom within a half-unit cell, the dashed curve represents the force expected on the Au atom trapped by the tip. This means that the tip-Au-surface junction is in region (ii), and this force is more attractive than the non-conservative force in region (iii). It is specious to relate the force minima at $z = 1.2$ Å to the force needed to maintain the atomic junction. In addition, the chemical bonding force between the tip and the Au atom which stably maintains the atomic junction at $z = 1.2$ Å is close to -0.6 nN. Since this value is comparable to a chemical bonding force [37], the INSAM mechanism can be attributed to a purely mechanical effect. At smaller tip-surface distances (in region (i)), the second force minimum appears in the short-range force curve. Atomic relaxations induced by the tip-Au-surface interaction should occur in this region. The configuration change caused the force minimum. As the tip is closer to the surface, second-layer atoms on the tip-apex contribute to the interaction, resulting in a more attractive force. The further increase of the dissipation signal at $z < 1.2$ Å is related to the onset of an additional dissipation channel, which stems from the tip apex or surface atom modifications [10, 57, 58]. This atomic junction is less stable than the junction formed in region (ii) because the repulsive force starts to act in region (i).

Acknowledgments This work was supported by a Grant-in-Aid for Scientific Research from the Ministry of Education, Culture, Sports, Science and Technology of Japan (MEXT), and by the Funding Program for Next Generation World-Leading Researchers.

References

1. T.R. Albrecht, P. Grütter, D. Horne, D. Rugar, J. Appl. Phys. **69**, 668 (1991)
2. S. Morita, R. Wiesendanger, E. Meyer (eds.), *Noncontact Atomic Force Microscopy* (Springer, Berlin, 2002)
3. F.J. Giessibl, Rev. Mod. Phys. **75**, 949 (2003)
4. M.A. Lantz, H.J. Hug, R. Hoffmann, P.J.A. van Schendel, P. Kappenberger, S. Martin, A. Baratoff, H.-J. Guntherodt, Science **291**, 2580 (2001)
5. Y. Sugimoto, P. Pou, M. Abe, P. Jelínek, R. Pérez, S. Morita, O. Custance, Nature **446**, 64 (2007)
6. M. Setvín, P. Mutombo, M. Ondráček, Z. Majzik, M. Švec, V. Cháb, I. Ošt'ádal, P. Sobotík, P. Jelínek, ACS Nano **6**, 6969 (2012)
7. S. Hirth, F. Ostendorf, M. Reichling, Nanotechnology **17**, S148 (2006)
8. Y. Sugimoto, P. Jelínek, P. Pou, M. Abe, S. Morita, R. Pérez, O. Custance, Phys. Rev. Lett. **98**, 106104 (2007)
9. M. Ternes, C.P. Lutz, C.F. Hirjibehedin, F.J. Giessibl, A.J. Heinrich, Science **319**, 1066 (2008)
10. Y. Sugimoto, P. Pou, O. Custance, P. Jelinek, M. Abe, R. Perez, S. Morita, Science **322**, 413 (2008)
11. Y. Sugimoto, K. Miki, M. Abe, S. Morita, Phys. Rev. B **78**, 205305 (2008)
12. O. Custance, R. Perez, S. Morita, Nat. Nanotechnol. **4**, 803 (2009)
13. A. Yurtsever, Y. Sugimoto, M. Abe, K. Matsunaga, I. Tanaka, S. Morita, Phys. Rev. B **84**, 085413 (2011)
14. A. Sweetman, S. Jarvis, R. Danza, J. Bamidele, S. Gangopadhyay, G.A. Shaw, L. Kantorovich, P. Moriarty, Phys. Rev. Lett. **106**, 136101 (2011)
15. H.Q. Mao, N. Li, X. Chen, Q.K. Xue, J. Phys. Condens. Matter **24**, 084004 (2012)
16. R. Pawlak, S. Fremy, S. Kawai, T. Glatzel, H. Fang, L.A. Fendt, F. Diederich, E. Meyer, ACS Nano **6**, 6318 (2012)
17. G. Langewisch, J. Falter, H. Fuchs, A. Schirmeisen, Phys. Rev. Lett. **110**, 036101 (2013)
18. L. Pizzagalli, A. Baratoff, Phys. Rev. B **68**, 115427 (2003)
19. U. Kurpick, T.S. Rahman, Phys. Rev. Lett. **83**, 2765 (1999)
20. A. Kuhnle, G. Meyer, S.W. Hla, K.H. Rieder, Surf. Sci. **499**, 15 (2002)
21. D.M. Eigler, E.K. Schweizer, Nature (London) **344**, 524 (1990)
22. N. Nilius, T.M. Wallis, W. Ho, Science **297**, 1853 (2002)
23. J.A. Stroscio, F. Tavazza, J.N. Crain, R.J. Celotta, A.M. Chaka, Science **313**, 948 (2006)
24. S. Loth, S. Baumann, C.P. Lutz, D.M. Eigler, A.J. Heinrich, Science **335**, 2012 (2012)
25. A.A. Khajetoorians, B. Baxevanis, C. Hübner, T. Schlenk, S. Krause, T.O. Wehling, S. Lounis, A. Lichtenstein, D. Pfannkuche, J. Wiebe, R. Wiesendanger, Science **339**, 55 (2013)
26. Y. Sugimoto, M. Abe, S. Hirayama, N. Oyabu, O. Custance, S. Morita, Nat. Mater. **4**, 156 (2005)
27. F. Ming, K. Wang, S. Pan, J. Liu, X. Zhang, J. Yang, X. Xiao, ACS Nano **5**, 7608 (2011)
28. Y. Sugimoto, A. Yurtsever, M. Abe, S. Morita, M. Ondráček, R. Pérez, P. Jelínek, ACS Nano **7**, 7370 (2013)
29. M. Abe, Y. Sugimoto, O. Custance, S. Morita, Appl. Phys. Lett. **87**, 173503 (2005)
30. M. Abe, Y. Sugimoto, T. Namikawa, K. Morita, N. Oyabu, S. Morita, Appl. Phys. Lett. **90**, 203103 (2007)
31. N. Oyabu, O. Custance, I. Yi, Y. Sugawara, S. Morita, Phys. Rev. Lett. **90**, 176102 (2003)
32. J.E. Sader, S.P. Jarvis, Appl. Phys. Lett. **84**, 1801 (2004)
33. I. Horcas, R. Fernandez, J.M. Gomez-Rodriguez, J. Colchero, J. Gomez-Herrero, A.M. Baro, Rev. Sci. Instrum. **78**, 013705 (2007)
34. S. Jarvis, A. Sweetman, J. Bamidele, L. Kantorovich, P. Moriarty, Phys. Rev. B **85**, 235305 (2012)
35. H. Uchida, D. Huang, F.m c Grey, M. Aono, Phys. Rev. Lett. **70**, 2040 (1993)
36. B.C. Stipe, M.A. Rezaei, W. Ho, Phys. Rev. Lett. **79**, 4397 (1997)

37. A. Yurtsever, Y. Sugimoto, H. Tanaka, M. Abe, S. Morita, M. Ondracek, P. Pou, R. Perez, P. Jelinek, Phys. Rev. B **87**, 155403 (2013)
38. P. Sharp, S. Jarvis, R. Woolley, A. Sweetman, L. Kantorovich, C. Pakes, P. Moriarty, Appl. Phys. Lett. **100**, 233120 (2012)
39. D.L. Klein, R. Roth, A.K.L. Lim, A.P. Alivisatos, P.L. McEuen, Nature **389**, 699 (1997)
40. V. Ray, R. Subramanian, P. Bhadrachalam, L.C. Ma, C.U. Kim, S.J. Koh, Nat. Nanotechnol. **3**, 603 (2008)
41. M. Haruta, N. Yamada, T. Kobayashi, S. Iijima, J. Catal. **115**, 301 (1989)
42. M. Haruta, Catal. Today **36**, 153 (1997)
43. M. Valden, X. Lai, D.W. Goodman, Science **281**, 1647 (1998)
44. T.D. Ladd, F. Jelezko, R. Laflamme, Y. Nakamura, C. Monroe, J.L. O'Brien, Nature **464**, 45 (2010)
45. J.-L. Li, J.-F. Jia, X.-J. Liang, X. Liu, J.-Z. Wang, Q.-K. Xue, Z.-Q. Li, J.S. Tse, Z. Zhang, S.B. Zhang, Phys. Rev. Lett. **88**, 066101 (2002)
46. S.-C. Li, J.-F. Jia, R.-F. Dou, Q.-K. Xue, I.G. Batyrev, S.B. Zhang, Phys. Rev. Lett. **93**, 116103 (2004)
47. Y. Sugimoto, A. Yurtsever, N. Hirayama, M. Abe, S. Morita, Nat. Commun. **5**, 4360 (2014)
48. C. Zhang, G. Chen, K. Wang, H. Yang, T. Su, C.T. Chan, M.M.T. Loy, X. Xiao, Phys. Rev. Lett. **94**, 176104 (2005)
49. Y. Sugimoto, Y. Nakajima, D. Sawada, K. Morita, M. Abe, S. Morita, Phys. Rev. B **81**, 245322 (2010)
50. K. Wang, C. Zhang, M.M.T. Loy, X. Xiao, Phys. Rev. Lett. **94**, 036103 (2005)
51. Y. Zhou, Q.H. Wu, H.Z.H. Zhou, C. Zhan, J. Kang, Surf. Sci. **602**, 638 (2008)
52. J.M. Gómez-Rodríguez, J.J. Sáenz, A.M. Baró, J.-Y. Veuillen, R.C. Cinti, Phys. Rev. Lett. **76**, 799 (1996)
53. G. Chizhov, I. Lee, R.F. Willis, Phys. Rev. B **56**, 12316 (1997)
54. Y. Wu, Y. Zhou, C. Zhou, H. Zhan, J. Kang, J. Chem. Phys. **133**, 124706 (2010)
55. N. Sasaki, M. Tsukada, Jpn. J. Appl. Phys. **39**, L1334–L1337 (2000)
56. L.N. Kantorovich, T. Trevethan, Phys. Rev. Lett. **93**, 236102 (2004)
57. N. Oyabu, P. Pou, T. Sugimoto, P. Jelinek, M. Abe, S. Morita, R. Perez, O. Custance, Phys. Rev. Lett. **96**, 106101 (2006)
58. A. Schirmeisen, D. Weiner, H. Fuchs, Phys. Rev. Lett. **97**, 136101 (2006)